

Short Communication

Preparation and Performance of Fe-based Amorphous Laser Cladding Layers on Low Carbon Steel

Lun Zhang^{1,2}, Shaoteng Jiang^{1,2}, Kaitian Mei^{1,2}, Huadong Qiu^{1,2}, Hui Zhang^{1,2,*}

¹ College of Mechanical Engineering, Qilu University of Technology (Shandong Academy of Sciences), 250353, Jinan, China

² Shandong Institute of Mechanical Design and Research

*E-mail: zhanghui198787@163.com

Received: 7 December 2021 / Accepted: 21 January 2022 / Published: 4 March 2022

Fe-based amorphous cladding layers were prepared on low carbon steel using synchronous powder feeding Fe-based amorphous powder. The formation of the Fe-based amorphous cladding layer was improved by optimising the laser cladding process parameters, which eliminated defects in layers such as cracks and pores and improved their properties. The results show that the cladding layer comprises amorphous, dendrite, and equiaxed grains. The hardness of the amorphous phase is about 1351 HV_{0.2}, the grain size of the fine dendrites is 1.43 μm and the hardness is 1273 HV_{0.2}. The average hardness of the overall cladding layer is 7.93 times, and the corrosion current density is ten times lower than that of the low-carbon steel substrate.

Keywords: Fe-based amorphous; corrosion resistance; laser cladding

1. INTRODUCTION

Laser cladding is commonly used for surface strengthening and repairing. It has the characteristics of rapid melting and solidification, low dilution, and simple operation [1-3]. The wear resistance and corrosion resistance of the substrates can be effectively improved by using this technology. Fe-based amorphous alloys usually have high hardness and wear resistance, and excellent corrosion resistance. However, it is challenging to prepare large areas [4-6]. Therefore, Fe-based amorphous alloys on a substrate surface can endow the components with excellent properties [7]. Compared to other amorphous alloys, Fe-based amorphous alloys use less rare metal elements, have lower material costs, and can be widely used in many fields.

The most common processes for preparing Fe-based amorphous alloy coatings are thermal spraying [8, 9] and plasma spraying [10]. Micro-holes and micro-cracks are often formed during amorphous coatings by thermal spraying, which affects their corrosion resistance. While preparing

amorphous coatings by plasma spraying, crystallisation often occurs because of the instability of the plasma arc. Laser cladding technology has significant advantages in preparing Fe-based amorphous alloy coatings due to its high energy density and fast cooling rate. Previous studies investigated the hardness [11], wear resistance [12-14], corrosion resistance, and other properties of Fe-based amorphous cladding layers by varying the scanning speed [15-17], adjusting the laser process [18], and changing the elemental composition [19]. The process parameters of laser claddings greatly influence the formation of amorphous coatings. Therefore, after optimising the process, this study intends to prepare an amorphous cladding layer with higher hardness and better corrosion resistance.

2. MATERIALS AND METHODS

The substrate material used was low carbon steel, with dimensions of 60 mm × 30 mm × 5 mm. IPG-YLS-10000 solid fibre laser processing equipment was used to create claddings from the Fe-based amorphous powder using synchronous powder feeding. The alloying elements of the amorphous powder include Fe, Mo, Cr, Co, C and B elements. The continuous-wave laser was used with laser power of 1000 W, scanning speed of 10 mm/s, powder-feeding rate of 9.3 g/min, defocusing amount of 20 mm, and shielding gas flow rate of 15 L/min.

An X-ray diffractometer (XRD-6100, Shimadzu) was used for the phase analysis; the working voltage was 40 kV, the current was 40 mA, and the scanning rate was 4°/min. The microstructure and corrosion morphologies of the cladding layers were observed using a scanning electron microscope (SU3500) and a Phenom Prox scanning electron microscope. The hardness of the cladding layers was tested by using a hardness tester (HXD-1000TMC) with a load of 1.96 N, and the holding time was 15 s. The top surface of the cladding layer is used for XRD testing and electrochemical testing. Polarization curves were measured in a 3.5 wt% NaCl solution at 298 K, with a scan rate of 0.5 mV/s, using a Gamry Interface 1000 electrochemical workstation. Similarly, the open circuit potential and electrochemical impedance spectrum were measured using this workstation. The EIS test frequency range was from 100000 Hz to 0.01 Hz, and the amplitude was 10 mV. A saturated calomel electrode was used as the reference electrode and a platinum electrode was used as the counter electrode.

3. RESULTS AND DISCUSSION

The macromorphology of the amorphous powder is shown in Figure 1(a), where the powder particle size is between 70–110 μm, and it is a spherical powder with a regular shape. The XRD diffraction patterns of the Fe-based amorphous powder are shown in Figure 1(b). The XRD pattern of the amorphous powder shows a steamed-bun peak in 2θ between 40° and 50°, indicating that the powder is primarily amorphous. However, sharp peaks appear at 2θ=35.5° and 2θ=39°, indicating that the powder exhibits a particular crystallisation phenomenon [20].

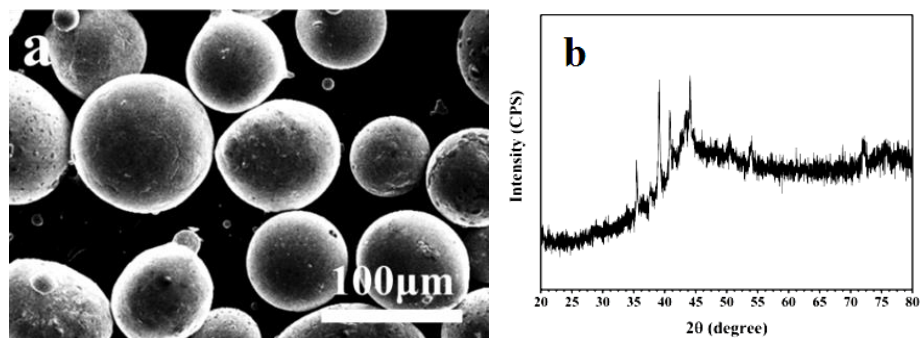


Figure 1. (a) Macro morphologies and (b) X-ray diffraction patterns of Fe-based amorphous powder

The macromorphology of the cladding layer is shown in Figure 2 (a) and can be seen to be well-formed macroscopically, without any apparent pores, cracks, or other defects. The phase of the cladding layer is mainly $\text{Co}_6\text{Mo}_6\text{C}$, along with Fe and Cr carbides $\text{M}_{23}(\text{C}, \text{B})_6$, and corresponds to the EDS analysis result of the amorphous powder.

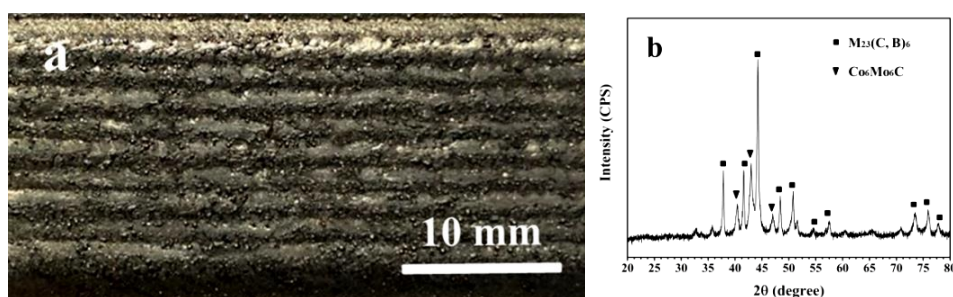


Figure 2. (a) Macromorphology and (b) X-ray diffraction patterns of the laser cladding layer

The microstructure of the cladding layer is shown in Figure 3. The Fe-based amorphous cladding layer comprises an amorphous phase, dendritic and equiaxed grains. Figure 3 (a) shows the amorphous phase and dendrites with larger sizes, where the dendrites are dispersed among equiaxed grains, and the average size of the larger dendrites is $1.91 \mu\text{m}$. Figure 3 (b) shows the fine dendrites and equiaxed grains, where the average particle size of the fine dendrites is $1.43 \mu\text{m}$. Figure 3 (c) is an enlarged view of region c in Figure 3 (b). The cooling rate of the non-overlap zone has reached the critical cooling rate for the formation of the amorphous phase. The remelting and reheating of the multi-pass laser cladding overlap zone is the main reason for grain formation and is an important factor affecting dendrite growth. Therefore, the main reason for forming equiaxed grains and dendrites is the insufficiently high cooling rate[21].

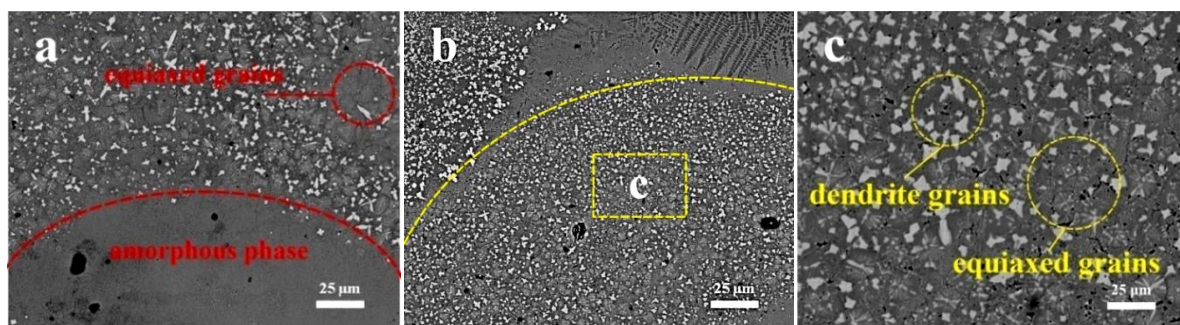


Figure 3. Secondary electron images of the cladding layer (a) amorphous phase equiaxed grains (b) fine dendrite and equiaxed grains (c) an enlarged view of region c in (b).

Figure 4 shows the microhardness of different structures in the cross-section of the cladding layer. The distribution of equiaxed grains and dendrites is consistent, and the remainder is amorphous. The microhardness of the amorphous phase can reach 1351 HV_{0.2}, which is 8.32 times that of the substrate. The average microhardness of the evenly distributed and fine dendrites is 1273HV_{0.2}, the average microhardness of the larger dendrites is 1236 HV_{0.2}, and the average hardness of the cladding layer is 1287 HV_{0.2}. Combined with Figure 2(b), the hardness of the amorphous phase and dendrite increases, primarily due to the formation of M₂₃(C, B)₆ and other carbides. In addition, Fe promotes the formation of equiaxed grains and dendrites, thereby reducing the hardness of the equiaxed grains region [22].

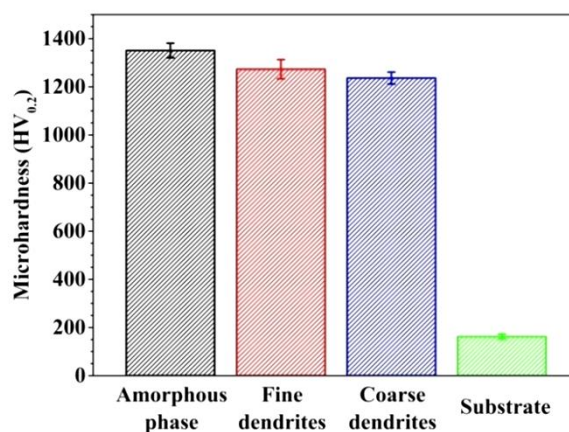


Figure 4. Microhardness of different microstructure in the cross-section of the cladding layer

Figure 5 (a) shows the open circuit potential curve of the cladding layer. When any corrosion starts, the open circuit potential of the coating begins to decrease and then tends to become stable. The potentiodynamic polarisation curves of the substrate and the cladding layer in a 3.5 wt% NaCl solution are shown in Figure 5 (b). The curves were fitted using the Tafel method, and the fitting results are shown in Table 1. The dispersed dendrites and equiaxed grains experience galvanic corrosion, which reduces the corrosion potential of the cladding layer. Compared to the mild steel substrate, the cladding

layer has a higher tendency toward thermodynamic corrosion. The current density of the amorphous cladding layer is $4.988 \mu\text{A}\cdot\text{cm}^{-2}$, which is more than ten times lower than mild steel, and the corrosion rate is also reduced by more than ten times. The polarisation curve in Figure 5 shows that when the corrosion potential is higher than -400 mV , the cladding layer becomes passivated, preventing further corrosion from occurring.

The main produced components of the passivation film are oxides of Mo and Fe [23]. In addition, the presence of the amorphous phase reduces grain boundary corrosion, thereby improving corrosion resistance. Wang et al. [22] performed laser remelting of the Fe-based amorphous cladding layer, and the corrosion potential of the obtained cladding layer in a 3.5 wt% NaCl solution was -0.539 V , similar to the findings of this study. However, the current density is 2.44 times the results derived in this study. Gao et al. [24] prepared a Fe-based amorphous cladding layer by plasma spraying, and the corrosion potential in the 3.5 wt% NaCl solution was -0.829 V and the current density was $33.3 \mu\text{A}\cdot\text{cm}^{-2}$. Compared to laser remelting and plasma spraying, the Fe-based cladding layer prepared in this study has better corrosion resistance. Figure 7(a) shows the corrosion morphology of the amorphous region after polarization. It can be seen that the amorphous area surface is relatively flat after corrosion. Figure 7(b) shows the equiaxed grains region where the dendrites are dispersed. Equiaxed grains are used as the anodes for galvanic corrosion. The grain boundaries are obviously corroded, while dendrite corrosion occurs slowly.

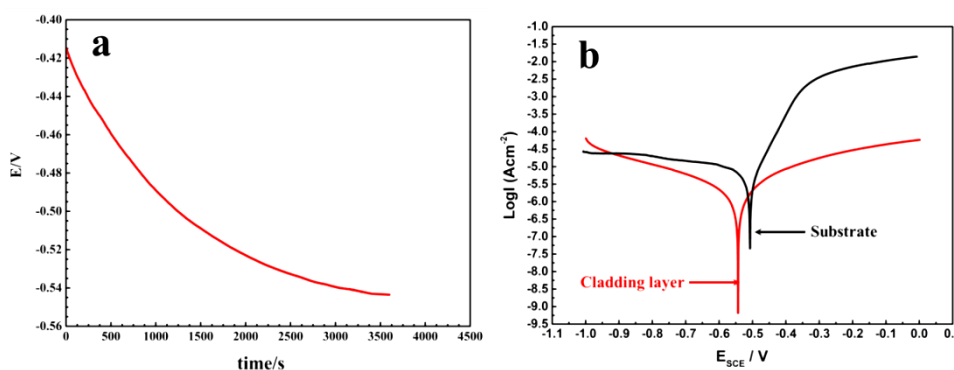


Figure 5. (a) Open circuit potential curve of the cladding layer and (b) Potentiodynamic polarization curves of the substrate and cladding layer in 3.5 wt% NaCl solution

Table 1. Fitting results of the potentiodynamic polarization curves of the substrate and cladding layer in 3.5 wt% NaCl solution

Samples	$E_{\text{corr}}(\text{V})$	$I_{\text{corr}}(\mu\text{Amp}/\text{cm}^2)$	Corrosion rate (mm/year)
Substrate	-0.508	53.12	0.6175
Cladding layer	-0.543	4.99	0.0580

The EIS Nyquist curve of the cladding layer is shown in Figure 6. Based on the equivalent circuit $R(\text{QR})(\text{QR})$ and the ZSmpWin software, the values of different components are reported in

Table 2. Here, R_s refers to the solution resistance, R_1 denotes the outer layer resistance of the cladding layer, and R_2 denotes the inner layer resistance of the cladding layer. The resistance of the outer layer of the cladding layer is $4747 \Omega\text{cm}^2$, and the resistance of the inner layer is $225.3 \Omega\text{cm}^2$, indicating that the surface of the cladding layer has excellent corrosion resistance.

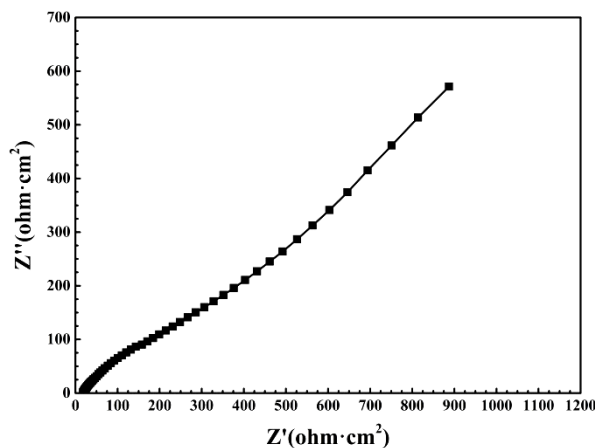


Figure 6. Electrochemical impedance Nyquist diagram of the cladding layer in 3.5 wt% NaCl solution

Table 2. Fitting results for electrochemical impedance Nyquist diagram of the cladding layer

	$R_s(\Omega\text{cm}^2)$	$R_1(\Omega\text{cm}^2)$	Q-Y0(μF)	Q-n	$R_2(\Omega\text{cm}^2)$	Q-Y0(μF)	Q-n
Cladding layer	17.27	4747	4206	0.5148	225.3	1119	0.5587

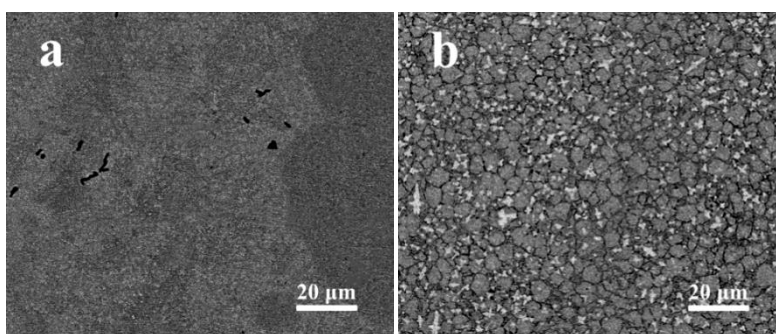


Figure 7. Corrosion morphologies of the cladding layer after running polarization tests (a) amorphous region (b) crystalline region

4. CONCLUSIONS

This study describes an amorphous alloy cladding layer that was successfully prepared on low carbon steel and was well-formed, without defects such as pores or cracks. The cladding layer comprised an amorphous phase, equiaxed grains, and dendrites, and the average dendrite size was $1.43 \mu\text{m}$. The average microhardness of the amorphous phase in the cladding layer is as high as 1350.67

HV_{0.2}, which is 8.32 times higher than the substrate. The corrosion rate of the cladding layer is more than ten times lower than the substrate.

ACKNOWLEDGMENTS

The work was supported by the Key Research and Development Program of Shandong Province (2019JZZY010418), the Shandong-Chongqing Science and Technology Cooperation Plan (2021LYXZ14), the Introduce Innovation Team Project of the City of Ji'nan (2019GXRC035), the integration project of Science-Education-Industry of Qilu University of Technology (Shandong Academy of Sciences) [2020KJC-GH12].

References

1. J. Chen, Y. Zhou, C. Shi, D. Mao, *Metals*, 7(2017)435.
<https://doi.org/10.3390/met7100435>
2. H. Liu, J. Hao, Z. Han, G. Yu, X. He, H. Yang, *J. Mater. Process. Technol.*, 232(2016) 153.
<https://doi.org/10.1016/j.jmatprotec.2016.02.001>
3. K. Wang, B. Chang, Y. Lei, H. Fu, Y. Lin, *Metals*, 7(2017)551.
<https://doi.org/10.3390/met7120551>
4. J. Do, S. Jung, H. Lee, B. Lee, G. Cha, C. Jo, S. Lee, *Metall. Mater. Trans. A*, 44(2013)2573.
<https://doi.org/10.1007/s11661-013-1615-0>
5. B. Wang, M. Jiang, Y. Xu, J. Hu, J. Wang, C. Zhou, *Jom.*, 72(2019)665.
<https://doi.org/10.1007/s11837-019-03927-5>
6. M. Yasir, C. Zhang, W. Wang, Z. Zhang, L. Liu, *J. Therm. Spray Technol.*, 25(2016)1554.
<https://doi.org/10.1007/s11666-016-0457-x>
7. Z. Chu, W. Deng, X. Zheng, Y. Zhou, C. Zhang, J. Xu, L. Gao, *J. Therm. Spray Technol.*, 29(2020)1111.
<https://doi.org/10.1007/s11666-020-01030-9>
8. N. Mahata, A. Banerjee, P. Bijalwan, P.K. Rai, S. Sangal, K. Mondal, *J. Mater.*, 26(2017)5538.
<https://doi.org/10.1007/s11665-017-2997-8>
9. S. Nayak, A. Banerjee, A. Kumar, T. Laha, *J. Therm. Spray Technol.*, 28(2019)1433.
<https://doi.org/10.1007/s11666-019-00907-8>
10. Y. Zhou, G. Ma, S. Chen, B. Fu, H. Wang, G. Li, *J. Therm. Spray Technol.*, 26(2017)1257.
<https://doi.org/10.1007/s11666-017-0582-1>
11. M. Yuan, Y. Wang, G. Xu, M. L. Qin, S. Liu, R. Jiang, Z. Liu, *Mater. Res. Innov.*, 18(2014)782.
<https://doi.org/10.1179/1432891714Z.000000000781>
12. H. Zhang, S. Wang, X. Yang, S. Hao, Y. Chen, H. Li, D. Pan, *Surf. Coat. Technol.*, 425(2021)127659.
<https://doi.org/10.1016/j.surfcoat.2021.127659>
13. J. Xu, J. Kang, W. Yue, Z. Fu, L. Zhu, D. She, *J. Non. Cryst. Solids.*, 573(2021)121136.
<https://doi.org/10.1016/j.jnoncrysol.2021.121136>
14. R. Li, W. Yuan, H. Yue, Y. Zhu, *Opt. Laser Technol.*, 146(2022)107574.
<https://doi.org/10.1016/j.optlastec.2021.107574>
15. X. Hou, D. Du, K. Wang, Y. Hong, B. Chang, *Metals*, 8(2018)622.
<https://doi.org/10.3390/met8080622>
16. M. Xiao, H. Gao, L. Sun, Z. Wang, G. Jiang, Q. Zhao, C. Guo, L. Li, F. Jiang, *Materials*, 297(2021)130002.
<https://doi.org/10.1016/j.matlet.2021.130002>
17. H. Wang, Y. Cheng, W. Song, J. Yang, X. Liang, *Intermetallics*, 136(2021)107266.
<https://doi.org/10.1016/j.intermet.2021.107266>

18. Y. Zhu, Z. Li, R. Li, M. Li, X. Daze, K. Feng, Y. Wu, *Appl. Surf. Sci.*, 280(2013)50.
<https://doi.org/10.1016/J.SURFCOAT.2021.127659>
19. K. Li, J. Liang, J. Zhou, *Surf. Coat. Technol.*, 423(2021)127520.
<https://doi.org/10.1016/j.surfcoat.2021.127520>
20. L. Jin, H. Zhou, Z. Huang, T. Zhang, X. Zhi, *Rare Metal Mater. Eng.*, 43(2019)1316.
<https://doi.org/10.13373/j.cnki.cjrm.xy18070028>
21. C. Jiang, H. Chen, C. Zhang, G. Wang, M. Dargusch, Y. Chen, Y. Xing, *J. Therm. Spray Technol.*, 26(2017)778.
<https://doi.org/10.1007/s11666-017-0546-5>
22. H. Wang, Y. Cheng, J. Yang, Q. Wang, *Surf. Coat. Technol.*, 414(2021)127081.
<https://doi.org/10.1016/j.surfcoat.2021.127081>
23. J. Jayaraj, Y. Kima, K. Kima, H. Seoka, E. Fleury, *J. Alloys Compd.*, 434-435(2007)237.
<https://doi.org/10.1016/j.jallcom.2006.08.288>
24. Z. Gao, J. Hao, J. Han, Y. Lu, Y. Chen, S. Li, *Surf. Coat. Technol.*, 44(2015)81
<https://doi.org/10.16490/j.cnki.issn.1001-3660.2015.01.026>

© 2022 The Authors. Published by ESG (www.electrochemsci.org). This article is an open access article distributed under the terms and conditions of the Creative Commons Attribution license (<http://creativecommons.org/licenses/by/4.0/>).